Statistical analysis of long GRBs' prompt emission and X-ray flares: multivariate clustering and correlations

Joseph Saji , Shabnam Iyyani , and Kratika Mazde¹

¹ Indian Institute of Science Education and Research, Thiruvananthapuram, Kerala, India, 695551

ABSTRACT

The extensive observations done by the X-ray telescope onboard Neil Gehrels Swift observatory has revealed the presence of late time flares concurrent with the decaying afterglow emission. However, the origin of these flares are elusive. In this work, we made use of the large database of Swift observations (2005 - 2020) of long GRBs to conduct a systematic statistical study between the prompt gamma ray emission and X-ray flares by characterising their temporal and spectral properties in terms of duration, quiescent period, peak flux, fluence, minimum variability timescale and spectral power-law index. The multi-dimensional database of parameters, thereby, generated was investigated by the principal component analysis which revealed there is no evident correlation between the different parameters of the prompt emission and X-ray flares. Furthermore, the correlation studies reveal that while there is a trend of positive correlation between the minimum variability timescale of flare and its duration, and a strong negative correlation with its peak flux, there are no such correlations observed in the prompt emission. Similarly, we find a positive correlation between the quiescent period and flare duration, and a negative correlation with the flare peak flux, while no such correlations are observed for the prompt emission of GRBs. Finally, among the X-ray flares, we find two dominant classes whose variations are driven by the minimum variability timescale, peak flux and fluences of the flares. A catalog of these different parameters characterising the prompt and flare emissions is presented.

Keywords: Gamma-ray bursts(629) — X-ray flares — Multivariate analysis(1913) — Astrostatistics techniques(1886) — Catalogs(205)

1. INTRODUCTION

Gamma ray bursts (GRBs) are characterised by two main events: firstly, the prompt emission which composes of the immediate gamma rays and secondly, the afterglow emission which composes of emission ranging from radio till gamma rays (Mészáros 2006; Kumar & Zhang 2015; Iyyani 2018). The quick autonomous re-pointing capability of *Neil Gehrels Swift* (Burrows et al. 2005a) spacecraft to the location of the burst, in particular, has enhanced the observations linking the prompt and X-ray afterglow emissions of GRBs. This is made possible by the onboard detectors, Burst Alert Telescope (BAT; Barthelmy et al. 2005) and X-ray Telescope (XRT; Burrows et al. 2005b) which make observations in the energy ranges $15-150\,\mathrm{keV}$ and $0.3-10\,\mathrm{keV}$, respectively.

One of the intriguing features of the gamma-ray bursts revealed by Neil Gehrels Swift observations is the presence of flares in the X-ray afterglow lightcurves. Systematic survey studies regarding the X-ray flares observed in Swift XRT were initially carried out by Chincarini et al. 2007a and Falcone et al. 2007. X-ray flares are found to occur in both long and short GRBs. This makes the flares a common feature in GRBs despite the difference in progenitors. Majority of the flares happen before a few 1000 s (Chincarini et al. 2007a), however, in a few of them, they are found to occur as late as $\geq 10^6$ s (Swenson et al. 2010; Kumar et al. 2022).

Spectral studies such as Morris 2008 using wider energy range combining data from BAT, XRT and UVOT¹ simultaneously available in a few cases have shown that the flare spectrum requires spectral models more complex than

Corresponding author: Shabnam Iyyani shabnam@iisertvm.ac.in

a simple power-law model of the afterglow radiation. This affirmed that the flares are distinctly different from the observed underlying afterglow emission. Several studies have been done to analyse various spectral and temporal properties of these flares observed in X-ray and optical in comparison with the prompt emission properties (Sonbas et al. 2013a; Peng et al. 2015; Yi et al. 2016, 2017; Liu & Mao 2019; Chang et al. 2021; Lü et al. 2022; Shi et al. 2022). The spectral studies have noted that the flares possess energy fluence comparable to that of the prompt emission (Burrows et al. 2005c; Falcone et al. 2007). In addition, multiple flaring episodes are also found in a certain fraction of GRBs (Chincarini et al. 2007a). As the flare durations tend to increases with time, the intensity of the flares are found to decrease with time.

Despite several studies, a self-consistent model explaining the origin, energetics and the evolution of the X-ray flares is yet to be developed. The various proposed models consider the following scenarios: (a) the late time flares are due to delayed central engine activity (MacFadyen et al. 2001; King et al. 2005; Margutti et al. 2011; Dall'Osso et al. 2017; Gibson et al. 2018); or if it is an extended phase of the prompt emission episode (Beniamini & Kumar 2016; Mu et al. 2016); or if it is the late time energy injection into the blast wave by refreshed shocks (Rees & Mészáros 1998; Laskar et al. 2015); or if it is the externals shocks propagating into a dense and uneven circumburst medium (Hascoët et al. 2017; Ayache et al. 2020).

In this work, we present a detailed multivariate statistical study of the temporal and spectral properties of the prompt and X-ray flare behaviours. Furthermore, a catalog of the studied properties are presented. Firstly, a reasonably large dataset based on the *Swift* observations is selected. Following which the parameters chosen to characterise the prompt and X-ray flare emissions are defined, and the methodology used to extract those features are described in the section 2. In section 3, the multivariate analysis including the distributions of the various parameters, principal component analysis, detailed correlation analysis cum modelling and clustering of X-ray flares are presented. Following, in section 4, we discuss and summarise the main results of the analysis and finally, present our conclusions.

2. SAMPLE SELECTION AND METHODOLOGY

The primary objective of the statistical analysis of different parameters of the prompt emission and X-ray flares of the GRBs requires a reasonably large dataset. The *Swift* observatory has been discovering approximately 100 bursts per year since 2004 and thereby, the large database including the prompt emission and late time X-ray flares observed by BAT and XRT respectively, provides the appropriate database for conducting the statistical studies. The afterglow lightcurves of all the long bursts (lGRBs)² detected by *Swift* XRT until May 2020 were manually examined to look for the presence of flares, which were also confirmed by the flare detection algorithm employed by *Swift* XRT team (Evans et al. 2009). After the primary inspection, 340 lGRBs (about 30% of the total *Swift* lGRBs observed during this period) were found to posses flaring activity during which the flux evolved in a manner differently from the otherwise continuously decaying afterglow behaviour. Among such identified flares, we further sorted and removed certain GRBs with the following light curve behaviours:

- incomplete flaring episodes such as either the rising or decaying phases of the flare light curve is completely absent,
- not enough observational data points available in the flare light curve such that it is insufficient for light curve characterisation,
- the immediate background emission in the regions pre or post the flare, that is the underlying afterglow emission, is absent or not enough observational data is available,
- small peaks in the lightcurve that are of very low signal-to-noise ratio³ ($\ll 0.1$) which are consistent with the statistical variation in the afterglow observations were strictly avoided⁴.

The above sorting resulted in the removal of about 35% of the initial sample and the final sample consisted of 220 lGRBs. Examples of the afterglow lightcurves of a few excluded GRBs using the above criteria, and selected GRBs with single, double and triple flaring episodes are shown in Appendix A.

 $^{^2}$ T_{90} represents the time duration within which 90% of the burst emission counts are detected by BAT. Long GRBs are those with $T_{90} \ge 2 \, s$.

³ Refer section 2.1 for definition.

⁴ Note: A very small number of bursts (less than 10) with 0.1 < SN ratio < 1 are included in the sample. In these cases, the parameters were measurable and we have included them in the database, so as to minimise selection biases.

2.1. Parameters of study

A schematic representation of the prompt emission and afterglow lightcurves consisting of late time X-ray flares is shown in the Figure 1a. The following parameters characterising the prompt and X-ray flare emissions of lGRBs are chosen for the study and reported in the catalog:

- $T_{P,100}$ & $T_{F,100}$: The total duration of the gamma-ray burst prompt emission and X-ray flare emission respectively.
- Fluence_P & Fluence_F: The total energy per cm² obtained after integrating the energy flux over the duration of the burst and flare respectively.
- Peak Flux, $F_{P,peak}$ & $F_{F,peak}$: The maximum energy flux that is recorded during the burst duration of prompt emission and X-ray flare (subtracting the underlying afterglow flux) respectively.
- Peak count time, $T_{P,peak}$ & $T_{F,peak}$: It marks the time when maximum count rate is observed in the prompt emission and X-ray flare light curves respectively.
- α_P & α_F : The low energy spectral index of the power-law spectra of the prompt emission and X-ray flare, respectively.
- Minimum variability timescale, $T_{P,var}$ & $T_{F,var}$: It describes the shortest time scale over which a significant change in the count rate of prompt emission and X-ray flare happens, respectively.
- Signal-to-Noise ratio of flare: Considering Poisson statistics, the signal-to-noise ratio of the flare is estimated as the ratio of the flare peak count rate (given as the total count rate afterglow count rate at the peak time) to the square root of the total count rate at the peak time. This measure helps to check how distinct and statistically significant the flare is from the underlying afterglow emission. In addition, the distribution of statistical significance allows to verify if the sample is biased or not.
- Quiescent period, T_q : It is the difference between the start time of the $T_{F,100}$ of the X-ray flare and the end time of the $T_{P,100}$ of the prompt emission. During this period, there are no source photon counts other than background noises in BAT and the underlying afterglow emission in the XRT.

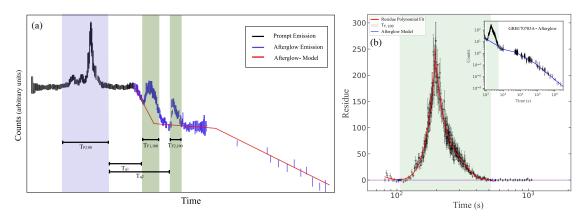


Figure 1. (a) A schematic representation of the GRB prompt emission and afterglow lightcurves including the late time X-ray flares. The temporal parameters, $T_{P,100}$, $T_{F,100}$ and quiescent period $[T_q]$ are marked. (b) Residue plot of GRB170705A showing polynomial fit in the rise and decay phases of X-ray flare is shown. The points at which the fit coincide with residue = 0 line are marked in blue squares. The afterglow(black) and its corresponding model(blue solid line) of the same GRB is shown in the embedded plot.

2.2. Methodology of Extracting the Parameters

In the following subsections, the methodology of how the above defined parameters are systematically extracted from the data is presented.

2.2.1. Prompt Emission Data Analysis

The prompt BAT light curves were analysed using the Heasarc script of Bayesian Block binning named as battblocks with ncp_prior = 6 and uniform time binning of 0.01s to estimate the total duration, $T_{P,100}$, and the peak time, $T_{P,peak}$ of the prompt emission of the burst. The time integrated and peak count BAT spectra of the burst were created for the duration of $T_{P,100}$ and for 1 second duration around $T_{P,peak}$ of the prompt emission in the energy range 15 – 150 keV, respectively. The spectral data were then analysed using the Multi-Mission Maximum Likelihood Framework (3ML, V.2.2.1, Vianello et al. 2015) software package. Using 3ML, the spectra were analysed using different phenomenological spectral functions such as simple power-law, cutoff power-law and Band function (Poolakkil et al. 2021). By comparing the Akaike Information Criterion (AIC)⁵, the spectral function fit with the minimum AIC was considered as the best fit spectral model. From the best fit model, the low energy power-law index, α of the time integrated spectrum and the total energy fluence were noted. The peak energy flux was estimated from the analysis of the peak spectrum generated around the peak time of the prompt emission.

2.2.2. X-ray Flare Data Analysis

The pre-processed XRT count rate light curves for the afterglow analysis were obtained from Swift XRT repository⁶ in the energy range, 0.3-10 keV. The binned GRB XRT afterglow light curves are ensured to contain at least 15 counts and the errors are calculated using the Gaussian statistics (Evans et al. 2009). The temporal structure of the afterglow emission consists of several power-laws of decaying count rate which is entirely different from the highly varying erratic pulses of emission in the flares (Figure 1a). Therefore, the first step in processing the data was to separate the two emissions. This was achieved by removing the rough data region that included the flares from the entire afterglow light curve and modelling the remaining smoothly decaying afterglow emission using a power-law or a combination of power-laws (Evans et al. 2007, 2009). The best-fit models were determined using the 3ML and AIC statistics. A multi-broken power-law model was found to best represent the underlying afterglow emission. The resulting best-fit model of the afterglow light curve was subtracted from the total afterglow emission, which produced a residual light curve including the propagated errors (Figure 1b). The peak count time of the flare was used to identify the rise and decay phase of the flare. Using the technique of fitting a polynomial function to the residual counts light curve, the respective last and first intersection points with the background curve in the rise and decay phases are selected as the start and the stop times of the flare episode respectively. The best fit polynomial for the rise and decay phases of the flare was selected after an iteration of polynomial fits of different orders and the one which gave the reduced chi-square closest to 1.

To ascertain the variation in the estimated start and stop times of the flare episode, 5000 MonteCarlo simulated residual light curves were generated by assuming a Gaussian distribution⁷ to each data point where the original residual count is the mean and its associated error as the standard deviation. The rise and decay phases in each residual light curve were analyzed using polynomial fits with the same best-fit order as the original residual light curve. The mean and standard deviation of the distributions of the start and stop times of the flare episode is referred to as $T_{F,start}$ and $T_{F,stop}$, and their associated errors respectively. The distribution of the duration of the flare episode was generated by taking the difference between the start and stop times of the flares of each simulated residual count curve. The mean and standard deviation of the distribution of the duration of the flare is reported as the $T_{F,100}$ and its associated error.

The X-ray flare spectrum was generated for the whole duration, $T_{F,100}$ of the flare in the energy range 0.3-10 keV using the Swift-XRT repository and analysed in 3ML. In order to separate the underlying afterglow emission, the X-ray spectra was firstly generated in regions selected pre and post of the X-ray flare or either one of them, depending on if enough data were available. The underlying afterglow emission spectra was first analysed using a power-law function multiplied by two absorption terms: galactic, n_H and source, n_H . The galactic, n_H , was chosen based on the right-ascension (RA) and declination (Dec) of each burst whereas, the source, n_H was left as a free parameter in the fit. The Galactic n_H values were obtained from the Galactic n_H calculator available at Swift science data centre⁸, which is based on Willingale et al. (2013). Thereafter, the X-ray spectra generated for the flare duration is analysed using two power-law functions multiplied by the absorption coefficients (source, n_H was fixed at the value obtained

⁵ AIC is the statistic estimator which is calculated using the formula: $2k - 2ln(\hat{L})$ where k is number of estimated parameters and \hat{L} is the maximum likelihood function.

 $^{^6}$ Data products are available in the link: <code>https://www.swift.ac.uk/xrt_live_cat/</code>

⁷ The assumption of Gaussian distribution is applied to each data point of count rate in the residual light curve, by taking into account that if in case the count rate takes a negative value during the simulation, it would still have a physical meaning implying that the afterglow emission is more dominant at that instance. In addition, count rate allows for fractional values.

⁸ https://www.swift.ac.uk/analysis/nhtot/

during the afteglow spectral fit). One of the power-law functions was frozen to the afterglow spectral fit values and the other power-law function was left free to model the flare spectrum. Thereby, using the flare power-law model, the respective energy flux and fluence in the energy range, 0.3-10 keV, were estimated. In addition, the spectral index, α_F , along with the above mentioned parameters were added to the database. The peak flux of flare corresponding to the peak time is calculated from the flux lightcurve obtained from the Swift-XRT repository after subtracting the average afterglow flux

In the current sample, there are GRBs with multiple episodes of X-ray flare emissions. The end of a flaring episode is defined when the decay phase of the light curve touches the background. The further rise after this instance or after certain period of quiescence is considered as the onset of the consecutive flaring episode (Figure 1a). Using this criteria, we identify multiple episodes of the flare. Out of the 220 GRBs in the sample, there are 44 GRBs which possess two flaring episodes and 4 GRBs with three flaring episodes. In 96 GRBs, late time X-ray flares were observed concurrently by the BAT and XRT detectors. In such cases, the emission observed in BAT exempting the X-ray flare detected in XRT, is considered as the prompt emission in our study. Therefore, the $T_{P,100}$ estimate in such cases considers only the burst duration of the first episode of radiation that is observed in BAT. The quiescent period, T_q for the various flaring episodes are respectively measured as the difference between the onset time of the flaring episode and the end time of the $T_{P,100}$ of the burst (Figure 1a).

2.2.3. Variability Measurement

One of the defining characteristics of gamma ray burst emission is its highly variable light curves observed during the prompt emission (MacLachlan et al. 2013). Interestingly, the X-ray flares also exhibit strong variability and erratic light curves (Sonbas et al. 2013b). The minimum timescale of variability is the minimum timescale over which there is a significant or reasonable change in count rate in the observed light curve. The study of the variability pattern can provide us the information regarding the size and location of the source region (Kobayashi et al. 1997).

In this work, the Bayesian block (BB) technique (Scargle et al. 2013) of binning the counts light curve to identify the minimum variability timescale of both the prompt as well as the X-ray flare emissions was employed. BB bins the light curve such that each time interval possess a constant Poisson rate. This methodology divides the light curve into various time intervals of dynamical time widths and signal-to-noise ratio and closely follows the true underlying variation in the emission (Burgess 2014; Vianello et al. 2018). The time interval with the minimum timescale is considered as the minimum variability (T_{var}) of the light curve. The light curves of prompt and flare emissions are analysed using the Bayesian Block binning method available in Astropy package (Astropy Collaboration et al. 2022) in python. In order to compare the estimated variability timescales of both the prompt and flares emissions of a GRB as well as between different GRBs in the sample, a common false alarm probability of $p_0 = 0.01$ is adopted throughout the analysis. The $p_0 = 0.01$ is found to be an optimal choice allowing to effectively capture the variabilities across different emissions and provides a confidence level of 99%. This approach, thereby, ensures a systematic analysis, avoiding the use of multiple configurations specific to different GRBs.

3. MULTIVARIATE ANALYSIS

In this section, we analyse the multi-dimensional database that is generated via the methodology described in the previous section to assess the probability distributions, correlation and clustering of the various studied parameters.

3.1. Distributions of prompt and X-ray flare parameters

The histogrammed probability density plots of the temporal and spectral related parameters of both the prompt and X-ray flare emissions studied for the GRBs in this work are presented in the Figure 2. In addition, the smoothed version of the distribution obtained via the kernel density estimation (KDE) using the Gaussian kernels are also shown.

The X-ray flare episodes have durations on average greater than that of the prompt emission and the consecutive flaring episodes tend to be even longer. The mean (median) of the prompt duration is around 51^{+117}_{-35} s (59 s), whereas the first and second X-ray flaring episodes, on average (median), have longer durations of 188^{+449}_{-133} s (169 s) and 344^{+1182}_{-267} s (230 s), respectively (Figure 2a and 2b). The average (median) quiescent periods of the first and second flaring episodes are found to be around 69^{+368}_{-58} s (91 s) and 303^{+593}_{-200} s (224 s), respectively (Figure 2c). One of the immediate similarities that can be noted between the prompt emission and the X-ray flares via a visual inspection is the erratic nature of both the light curves which is quantified using variability timescale measurements. The prompt emission light curves exhibit minimum variabilitPrompt emission and X-ray flaresies over time scales on average (median) $2.7^{+13.4}_{-2.2}$ s (2.4 s),

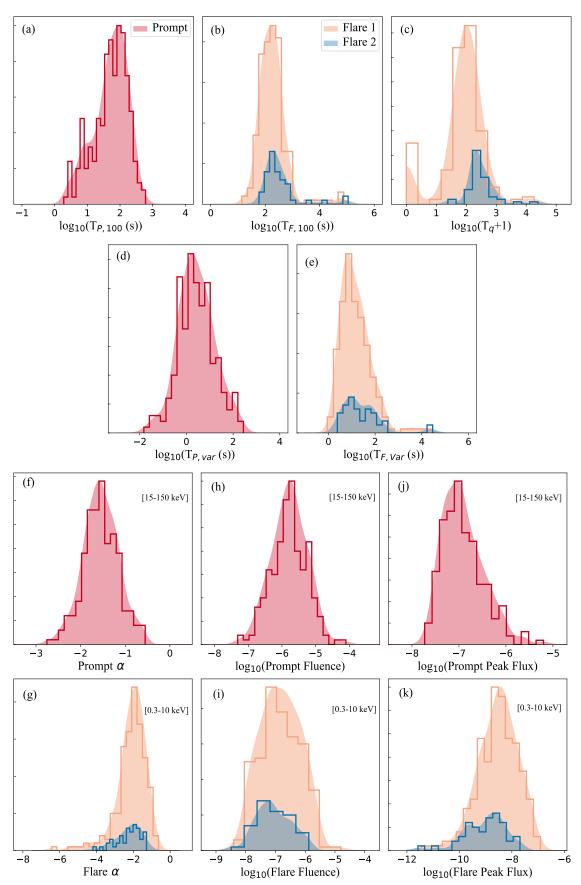


Figure 2. The distributions obtained for the prompt (red) and flare (orange for first flare episode and blue for second flare episode) temporal parameters are shown. The vertical bars represent the histograms and the respective KDE curves are shown in color filled shaded curves. The distributions of a) $T_{P,100}$, b) $T_{F,100}$, c) T_q , d) $T_{P,var}$, e) $T_{F,var}$, f) α_P , g) α_F , h) Fluence_P, i) Fluence_F, j) $F_{P,peak}$, and k) $F_{F,peak}$ are shown.

see Figure 2d, while the minimum variability timescales of first and second X-ray flare episodes are relatively of longer durations on average (median) 15^{+56}_{-12} s (11 s) and 25^{+144}_{-22} s (16 s), respectively (Figure 2e). We note that X-flare light curves depending on the exposure times, for majority of first episodes an average 1 s time resolutions were available, but, in some cases, the time resolutions were longer.

The low energy power-law spectral indices, α_P for the time integrated spectrum of the total prompt emission duration (energy band: 15 - 150 keV) are found to be on average (median) around -1.5 ± 0.40 (-1.5), see Figure 2f. However, the lower energy power-law spectral indices, α_{F1} and α_{F2} of the time integrated spectrum of the total first and second X-ray flare episodes in energy range 0.3 - 10 keV are on average (median) much softer, around -2.1 ± 0.83 (-2.0) and -2.25 ± 0.65 (-2.17), respectively (Figure 2g).

The fluence and the peak flux of the prompt episode is on average (median) around $1.6^{+3.8}_{-1.1} \times 10^{-6}$ (1.7×10^{-6}) erg/cm² and $1.2^{+2.1}_{-0.78} \times 10^{-7}$ (1.1×10^{-7}) erg/cm²/s, respectively in the energy range 15 - 150 keV (Figures 2h and 2j). The average (median) of the fluence of the first and second X-ray flaring episodes in 0.3 - 10 keV is around $1.5^{+5.2}_{-1.1} \times 10^{-7}$ (1.5×10^{-7}) erg/cm²/s and $8.7^{+24.7}_{-6.5} \times 10^{-8}$ (7.2×10^{-8}) erg/cm², respectively (Figure 2i). The first and second episodes of the X-ray flare episodes have peak flux on average (median) around $2.9^{+14}_{-2.4} \times 10^{-9}$ (3.2×10^{-9}) erg/cm²/s and $9.3^{+47}_{-7.8} \times 10^{-10}$ (1.2×10^{-9}) erg/cm², respectively (Figure 2k).

3.2. Principal component analysis

Principle Component Analysis (PCA) allows to search for trends or correlations between parameters and sort them based on their contribution to the observed variance in the data. The PCA of the entire multi-dimensional dataset including the parameters of both prompt and X-ray flares, thereby, gives us some insight into the relation between different parameters and also shows the parameters that mainly drive the variability in clustering. PCA reduces the multi-dimensionality of the dataset into a few principal components which is a linear combination of the original parameters. We find that principal component 1 (PC1) and principal component 2 (PC2) together account for 46% of the total variability in the dataset. Using PC1 and PC2, the PCA circle of correlation is created as shown in Figure 3a. Here the correlation refers to the Pearson correlation coefficient between the parameter and the principal components. Thereby, the parameters that are positively correlated among each other are grouped together within the same quadrant and if they are negatively correlated the parameters would be positioned in opposite quadrants. The parameters that are less correlated with each other would be positioned in adjacent quadrants and would be at nearly right angles to each other. It is also key to note that the length of each vector variable from the origin (centre of the circle) in the plot represents the quality of representation of the variable. In other words, it represents the percentage of the contribution of that parameter in defining the PCA axes 1 and 2 combined, which is provided in the contribution color bar shown in the Figure 3a.

With the above understanding, from the PCA analysis⁹ of the dataset, we find there exists no explicit correlation between the temporal and spectral parameters of prompt emission and X-ray flares, as evident from Figure 3a. In case of α and T_{var} , it is important to note that the quality of representation of these parameters on PC1 and PC2 are lowest and therefore, their degree of correlations may not be strong (see section 3.3 for more details). Using this initial results of PC analysis as a guide, we look into the correlations between the various parameters and clustering in the subsequent sections in detail.

3.3. Correlation Analysis

The correlation analysis explores and identifies trends, patterns or relationships between different parameters under consideration, including positive, negative or no correlation. This can be quickly assessed by visualizing data in a scatter plot. Most importantly, correlation does not imply direct causation, as the relationship between parameters may be complex. Nonetheless, a correlation does indicate interdependence, allowing for further exploration of the underlying physical scenario.

A Pearson Correlation Matrix of the various parameters of the prompt emission and the first and second X-ray flare episode is shown in Figure 3b. The correlation matrix features markers indicating the various levels of statistical significance, including p-value < 0.001, p < 0.01, p < 0.05, and p > 0.05. The p-value represents the probability of the null hypothesis which considers there is no correlation between the variables and thereby serves as the measure of the statistical significance of accepting the alternate model i.e there exists a correlation between the two variables. The

⁹ For the PC analysis, the R package FACTOMINER (Lê et al. 2008) was used.

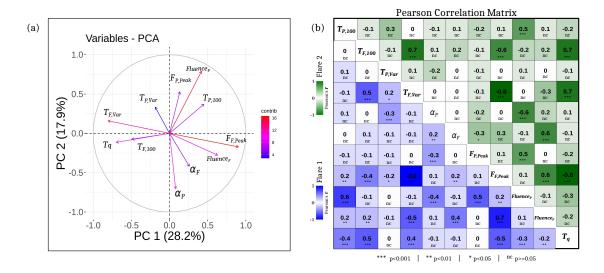


Figure 3. (a) PCA circle of correlation showing the relationship between all the prompt and X-ray flare parameters is shown. The percentage of the total contribution of each parameter to the PCA axes is represented by the color coding. (b) The Pearson Correlation Matrix of the various parameters of the prompt emission and the first (blue), and second (green) X-ray flare episodes are shown. Markers representing the p-values of the obtained correlations are shown in each cell representing the statistical significance of the correlation.

parameters of the third flare episodes are not included in the correlation matrix because only a small fraction of the sample consisted of such multiple flaring episodes. However, they are included in the detailed correlation plots and modelling. In this work, we have modelled only those correlations between parameters that exhibited a positive or negative Pearson correlation coefficient > 0.5, both in first and second flaring episodes. All the modelled correlations in our investigation demonstrate strong statistical significance as indicated by the low p-values, less than 0.001.

In Figure 4a, the duration of the X-ray flare, $T_{F,100}$, is plotted against the duration of the respective prompt emission, $T_{P,100}$, of the GRB. No particular correlation can be observed. For the purpose of comparison, the identity line representing when $T_{P,100} = T_{F,100}$ is marked. The duration of the flares including both first, second and third episodes of emission largely lie above this identity line suggesting that the flaring episodes tend to have durations greater than their respective prompt emissions. In addition, in case of multiple episodes of flaring, the consecutive episode is always longer than the preceding episode of flaring.

As evident from the Figure 4b, the flare minimum variability does not show any explicit correlation between the temporal properties of the prompt emission properties such as its minimum variability and duration (see Figure 3b). In comparison to the quiescent period, there is only a trend of positive correlation between $T_{F,var}$ and T_q , with a weak Pearson correlation coefficient of +0.4 (Figure 3b). The minimum variability timescale of the flares is compared with the total duration of the flare as shown in Figure 4c. We note there is a positive correlation between $T_{F,var}$ and $T_{F,100}$ as follows

$$log_{10}T_{F,var} = (+0.71 \pm 0.06) log_{10}(T_{F,100}) - 0.42 \pm 0.15$$
(1)

We note that this positive correlation is a weak trend as we are limited by the small number of flares with very long durations (> 1000 s). Thus, this correlation can be affirmed in the future with increased detections of flares with longer durations and lightcurves with smaller time resolutions. Interestingly, in contrast to this behaviour of flares, we note that there exists no significant correlation between the prompt emission minimum variability and its duration (Figure 4d) as evident from the Pearson correlation matrix shown in Figure 3b. For a small number of GRBs, the BB binning of prompt emission resulted in minimum timescale equivalent to the whole burst duration (Figure 4d).

A positive correlation is found between the quiescent period, T_q , and the X-ray flare duration, $T_{F,100}$ (Figure 4e). The positive correlation is modelled using a linear fit in the log-space as follows

$$log_{10}(T_q + 1) = (+0.97 \pm 0.05) log_{10}(T_{F,100}) - 0.12 \pm 0.10$$
(2)

and is shown in solid red line in Figure 4e. In comparison, there is only a weak trend of negative correlation observed between the quiescent period and the prompt emission duration of the bursts as shown in Figure 4f.

The prompt and flare emission spectra were modelled using the BAT and XRT data, obtained in the energy ranges 15-150 keV and 0.3-10 keV respectively. For the purpose of comparison of spectral behaviours, we assumed that the obtained prompt spectral model remains the same in the extrapolated lower energy range of 0.3 - 10 keV and thereby, studied the correlations between the spectral properties of the prompt and flare emissions.

Firstly, we studied the correlation between the low energy power-law index (α_P) of either the power-law or the cutoff power-law model used to best model the time integrated prompt spectra in the energy range 15 – 150 keV and the low energy power-law index (α_F) of the power-law model that was used to model the time integrated flare spectra in the energy range 0.3 – 10 keV, as shown in the Figure 5a. There is no explicit correlation observed between the α_F and α_P . For majority of the sample the α_F tends to be much softer than α_P .

The high energy (> 10 keV) part of the flare spectrum is not available for analysis and therefore, the peak of the flare spectrum is not known. It has been observed in the prompt emission that the spectral peaks are typically around a few hundred keVs. Therefore, for the purpose of comparing the energy fluxes between the prompt and flare, we estimate the prompt flux expected in the energy range 0.3 -10 keV by extrapolating the spectrum obtained from the analysis in the 15 -150 keV to those energies. In Figure 5b, we have compared the peak fluxes of both prompt and X-ray flare estimated in the energy range for 0.3-10 keV. Again, no significant correlation between these parameters are found. The flares are found to be less brighter than the prompt emission, Figure 5c. We further note that among the multiple flaring episodes of the GRB, the subsequent flaring episodes are found to be less intense as evident in Figure 5d. This is consistent with the findings by Chincarini et al. (2007b) and Falcone et al. (2007).

The prompt emission do not show any correlation between its peak flux and its duration (Figure 5e). However, it is interesting to note that the flare peak flux shows a weak trend of negative correlation (Pearson correlation coefficient = -0.42) with flare duration (Figure 5f). Similarly prompt emission does not show any significant correlation between it's peak flux and minimum variability and the quiescent period (Figure 5g and 5i). However, the peak flux of X-ray flare shows significant negative correlation between its minimum variability and quiescent period (Figure 5h and 5j) where modelling is given as follows:

$$log_{10}(F_{F,peak}) = (-0.89 \pm 0.05) log_{10}(T_{F,var}) - 7.44 \pm 0.06$$
(3)

$$log_{10}(F_{F,peak}) = (-1.05 \pm 0.07) log_{10}(T_q + 1) - 6.39 \pm 0.17$$
(4)

Certain GRBs among the sample show the occurance of flaring partly or fully during the plateau phase of the afterglow emission (Appendix A). The plateau phase is considered to be the region where the power law slope of the afterglow ranges between +/- 0.3. We have identified 13 GRBs wherein 12 of them have either first or all episodes of flares occurring partly or fully during the plateau phase while only one case (GRB110414A) has its second episode of flaring alone, occurring during the plateau phase. These GRBs are particularly highlighted in all the correlation plots. We note that these GRBs do not exhibit any unusual trend in the correlation studies in comparison to the other GRBs in the sample.

3.4. Clustering

It is observed that among the GRB population only certain GRBs possess X-ray flaring episodes and among them certain GRBs are found to have multiple episodes of flaring, some with and without quiescent periods etc. Such variability among the different GRBs suggest the possibility of the existence of subgroups among the GRBs with X-ray flaring.

No major dissimilarity is observable between the distribution of the properties of the prompt emission of GRBs with and without flares, see Appendix B. In addition, the Kolmogorov–Smirnov (KS) test shows that it is highly likely that GRBs with and without X-ray flares belong to the same population. The Principle component analysis done in section 3.2 shows that there is no explicit correlation between the studied prompt and flare properties. Therefore, we incorporated only the X-ray flare properties to investigate the possibility of clusters among the flaring GRBs. This included the following X-ray flare parameters: $T_{F,100}$, $T_{F,var}$, T_q , Fluence_F, $F_{F,Peak}$ and α_F .

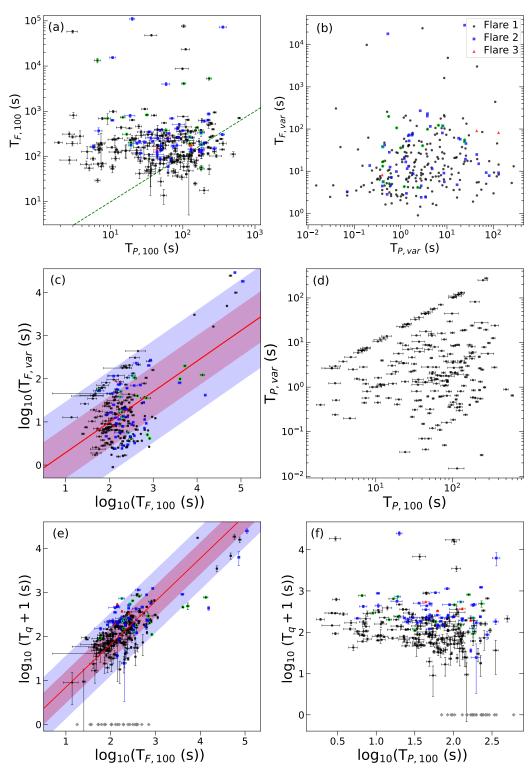


Figure 4. (a) $T_{F,100}$ is plotted against $T_{P,100}$. The black circles, blue squares and red triangles represent the first, second and third X-ray flaring episodes, respectively. The same color code and markers are used hereafter. The green dashed line represents when $T_{P,100} = T_{F,100}$. (b) The $T_{F,var}$ is plotted against the corresponding $T_{P,var}$. (c) The $T_{F,var}$ is plotted against $T_{F,100}$. The linear fit in the log space is shown by red solid line. The shaded red and blue regions correspond to 1σ and 2σ deviations of data from the fit. The color code represents the same contours hereafter. d) $T_{P,100}$ is plotted against $T_{P,var}$ (e) T_q is plotted against $T_{F,100}$ in the left hand panel and (f) against $T_{P,100}$ in the right hand panel respectively. Note that the grey diamonds represent the GRBs with quiescent period equal to zero, are not included in the modelling of the correlation. The parameters of flares that occur during the plateau phase of the afterglow is marked in green unfilled circle and square markers for the first and second episodes of flare respectively

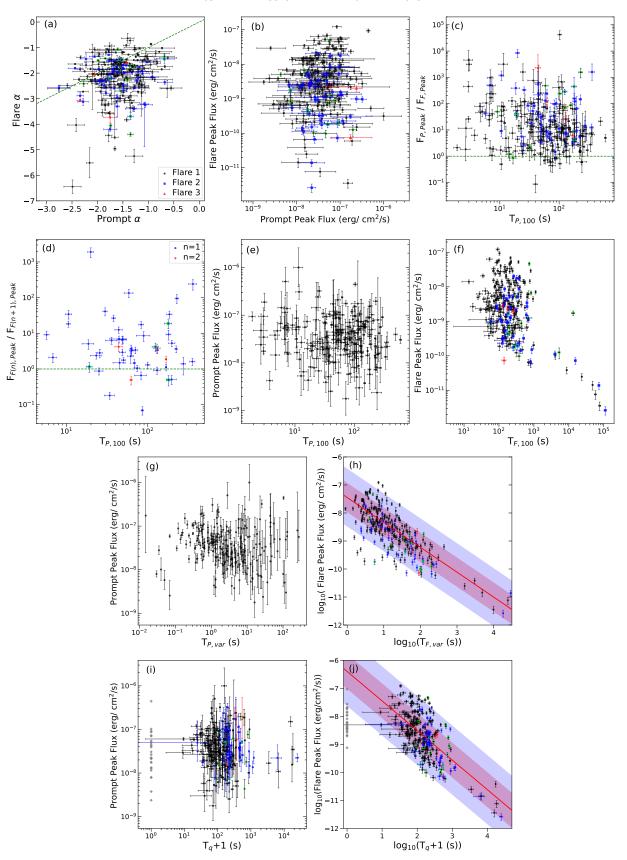


Figure 5. (a) α_P is plotted against α_F . (b) $F_{P,peak}$ is plotted against $F_{F,peak}$. (c) The ratio of $F_{P,peak}$ to $F_{F1,peak}$ and $F_{F2,peak}$ is plotted against the $T_{P,100}$ in black circles and blue squares respectively. (d) The ratio of $F_{F1,peak}$ to $F_{F2,peak}$ is plotted against $T_{P,100}$ in blue circles and the ratio of $F_{F2,peak}$ to $F_{F3,peak}$ in red circles. (e) $F_{P,peak}$ is plotted against $T_{P,100}$. (f) $F_{F,peak}$ is compared against $T_{F,100}$. (g) $F_{P,peak}$ is plotted against $T_{P,var}$. (h) $F_{F,peak}$ is compared against $T_{F,var}$. (i) $F_{P,peak}$ is plotted against T_{q} . (j) $F_{F,peak}$ is compared against T_{q} . The linear fit modelling the correlations in (h) and (j) are shown in red solid lines. The parameters of flares occurring during the plateau phase of the afterglow are highlighted in green unfilled circle and square markers for the first and second episodes of flare respectively.

Unsupervised clustering was carried out using Gaussian Mixture Model (GMM), Hierarchical and K-means algorithms¹⁰. To account for the large difference between numerical values of each parameters in the dataset, the data was standardised to a fixed order of range. All the chosen parameters except α_F is converted to log scale and later the complete dataset is scaled and centered by subtracting each values by their mean and dividing them by their standard deviation. The standardised dataset was then fed into the different clustering algorithms.

Based on the various evaluation metrics such as Silhouette score, Davies-Bouldin Index and Calinski-Harabasz Index, the K-means was found to be the best clustering algorithm for the dataset. The number of clusters in K-means were determined by two methods: Silhouette score (Rousseeuw 1987) and the Elbow method. The elbow was found to be at 4, signifying 4 possible subgroups within the GRBs with X-ray flares and the Silhouette score also peaked at 4 number of clusters. The obtained clusters are visualised in the principal component space as shown in Figure 6a. For understanding the origin of the clusters, we have marked the cases that had $T_q = 0$ in squares, GRBs with multiple flaring episodes with star markers and GRBs with flare in the plateau region of afterglow with yellow triangle marker. Since the T_q 's contribution in the PCA analysis is the largest in the fourth principal component, for the purpose of better visualising of the clusters, we chose to plot the clusters using PC4 versus PC1 in Figure 6a. The average values of the parameters of each of the cluster is reported in the Table 1. The GRBs with flares during the plateau are found across the clusters and does not display any discernible peculiar behaviours.

4. DISCUSSIONS AND CONCLUSIONS

The origin of the late time X-ray flares is largely a mystery. Owing to the similar erratic behaviour of the lightcurves, the prompt emission and X-ray flares, they are believed to be powered by the central engine. Therefore, in this work using the extensive database of *Swift* observations of both prompt and X-ray flares via BAT and XRT instruments onboard respectively, we performed a systematic statistical study of the various temporal and spectral parameters characterising these two emissions. The sample consisted of 220 long GRBs. Among them 172 GRBs possessed single episodes of flare emission, whereas, 44 and 4 GRBs had double and triple flaring episodes respectively. Among all the GRBs in the sample, 96 GRBs had their flaring episode observed synchronously in BAT as well. The temporal properties of the prompt and X-ray flare emissions were characterised by parameters such as total duration, minimum variability and the quiescent period between the episodes; and their spectral properties were characterised by parameters such as the low energy spectral power-law index, peak energy flux and energy fluences.

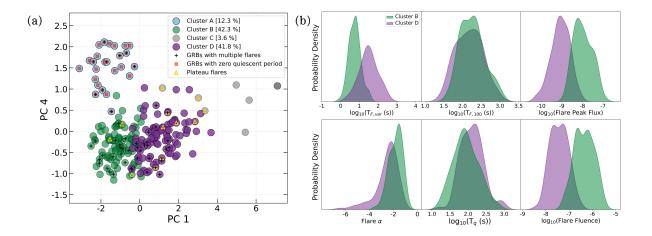


Figure 6. (a) The K-means clustering results are visualized in a PC plot. Black—cross and red—square markers represent the GRBs which posses multiple flares and GRBs with zero quiescent period respectively. The yellow triangle markers represent GRBs with flares in the plateau region of afterglow. (b) The KDE distributions of the various flare properties of the cluster B and D are shown.

¹⁰ The clustering packages available in scikit-learn (Pedregosa et al. 2011) were used.

	Cluster A	Cluster B	Cluster C	Cluster D
$\log_{10}(T_{F,100})$	2.08 ± 0.46	2.26 ± 0.32	4.26 ± 0.49	2.18 ± 0.35
$\log_{10}(T_{F,var})$	0.97 ± 0.42	0.76 ± 0.31	3.14 ± 0.91	1.49 ± 0.49
$lpha_F$	-1.87 ± 0.59	-1.81 ± 0.56	-1.64 ± 0.56	-2.54 ± 0.95
$\log_{10}(\mathrm{F}_{F,peak})$	-8.18 ± 0.43	-7.97 ± 0.44	-10.39 ± 0.84	-9.05 ± 0.44

 -6.59 ± 0.49

 0.07 ± 0.26

12.3~%

 $\log_{10}(\text{Fluence}_F)$

Cluster size (% of population)

 $\log_{10}(T_q)$

Table 1. Cluster Statistics

 -6.33 ± 0.41

 1.95 ± 0.35

42.3 %

 -6.70 ± 0.82

 3.54 ± 0.70

3.6%

 -7.42 ± -0.39

 2.11 ± 0.31

41.8 %

The distributions of the total duration of prompt and flaring episodes show that the flares largely have longer durations than the prompt with the median of $T_{F,100}$ distribution being nearly 3 times the median of $T_{F,100}$ distribution. The consecutive flaring episodes are found to be longer than the preceding one. The median of distribution of the duration of the second flaring episode is around 1.3 times the first episode of flare. This is consistent with the earlier studies done by Chincarini et al. (2007b).

The distribution of the minimum variability timescales of the prompt emission has a median around 2 s. On the contrary, the X-ray flare emissions tend to have larger variability timescales with a median of 12 s. The quiescent period between the prompt emission and the flaring episodes are found to range from none to around a day. The average of quiescence for the first flaring episode is around 100 s. The spectral parameters such as the low energy power-law index in the flares is found to be much softer than the prompt emission. The study of the energy fluence and peak energy flux show that the prompt emission is more intense and brighter than the X-ray flaring episodes when compared in the same energy range of 0.3 - 10 keV.

The principal component analysis and the correlation studies carried out on the dataset reveals that there is no explicit correlation between the prompt and X-ray flare properties in general. The duration of the prompt and flare episodes are uncorrelated. Interestingly, a positive correlation is observed between the quiescent period and the flare duration, while there is no significant correlation with the prompt emission duration. This implies that the property which drives the quiescent period and the onset time of the flare emission after the prompt has ended, is intrinsically connected with the origin of the flare, while it is less dependent on the prompt emission.

The minimum variability timescale observed in GRBs can point towards the size of the emitting region as well as allows one to understand the central engine activity, the impact of the circumburst medium as the jet propagates through the stellar core etc. There is no explicit correlation observed between the minimum timescale of variabilities of flares and that of prompt emission of the GRB. While there is no correlation between the prompt emission minimum variability and its duration, we find that there is a trend of positive correlation between the flare variability and its duration.

We compared the spectral properties of prompt and flare in the energy range 0.3 - 10 keV. This was done by extrapolating the spectrum obtained for prompt in the energy range 15-150 keV into the X-ray flare energy range of 0.3-10 keV. We find that the low energy power-law spectral index, α obtained for the spectrum of the total duration of prompt and flare respectively are found to be largely uncorrelated. The flare largely tends to have relatively much softer spectra in comparison to prompt. This may be attributed to the relatively longer duration of flares and may also point towards more rapidly evolving spectral behaviour in flares in comparison to prompt. We also find that the peak fluxes of prompt and flare emissions in the energy range 0.3-10 keV are uncorrelated. Consistent with previous studies (Falcone et al. 2007), the peak flux of the flare emission are found to be less brighter than the prompt and also decreases with consecutive flaring episodes. There is no explicit correlations observed between the peak fluxes of either of the prompt or flare and its durations. Interestingly, we also note that though there is no explicit correlation observed between prompt emission's minimum variability timescale and its peak flux, however, there exists a strong negative correlation between the flare's minimum variability timescale and its peak flux.

Further, using the flare properties alone, we explored the variety of classes among the current dataset of flares defined in this paper. Using K-means clustering algorithm, four clusters are found to exist. Among the clusters, we note that there is no preferential clustering for GRBs with multiple episodes of flares and are found to be spread across clusters. Among them we note that cluster A represents all 25 cases of flares which have zero quiescent period (Figure 6a). Thus, we conclude that the segregation of these X-ray flare events from the rest of the flare sample point out that

these observed flaring episodes are actually the continuing prompt emission. Among the remaining classes, we note that cluster C contains only 3.6% of the total sample and represents largely the flares with extreme values of duration, minimum variability timescale etc. This reduces the clustering to largely two main clusters B and D, each consisting $\sim 42\%$ of the sample. While inspecting the distributions of the various properties of these two clusters, we find that the segregation is largely driven by minimum variability timescale, peak flux and fluence as evident from the Figure 6b. Certain GRBs in the sample exhibit flaring during the plateau phase of the afterglow, but they do not display any unusual trends in correlation studies and are distributed across clusters without any discernible peculiar behaviours.

Thus, to summarise, in order to understand the origin of the prompt and X-ray flares, we find the following results of the correlation study: (a) no explicit correlation between the temporal and the spectral properties of the prompt and flare emissions; (b) there exists a trend of positive correlation between minimum variability timescale of flare and its duration, while there is a strong negative correlation between the minimum variability timescale of flare and it peak flux. However, there are no such trends to be found in the prompt emission properties; and, (c) there also exists a positive correlation between quiescent period and flare duration, and a negative correlation between the quiescent period and the flare peak flux, however, no such correlations are observed for the prompt emission of GRBs.

Therefore, using the current parameter characterisation of the prompt and X-ray flares adapted in this work, we do not find any significant evidence for the common origin for prompt emission of GRBs and the X-ray flares observed during the afterglow emission. In addition, we find the X-ray flares dominantly possess two main classes whose differences are primarily driven by the variability timescale, peak flux and fluences. Finally, we present the catalog of the estimated parameters to the community for further use in Appendix C.

One of the major future prospects of this work is to develop an understanding of the physical scenario leading to the observed correlations between late-time X-ray flares and the prompt emission. Furthermore, for a better comprehensive picture of the origin of flares, an extensive comparative study need to be carried out between the flares observed in X-rays and optical as well as high energy emission (> 100 MeV). The upcoming Cherenkov Telescope Array (CTA, Kakuwa et al. 2012) holds promise for further insights. We further note that a significant fraction of the initial sample had to be excluded due to incomplete data. An enhanced sample can be studied by adopting a light curve reconstruction method, similar to the one proposed in Dainotti et al. (2023) as increased sample size can lead to more confident assessments of the correlations presented in this study.

We thank the anonymous referee for valuable comments and suggestions. J.S. and S.I. are supported by DST INSPIRE Faculty Scheme (IFA19-PH245). S.I. is also supported by SERB SRG Grant (SRG/2022/000211). This research has made use of data obtained from the High Energy Astrophysics Science Archive Research Center (HEASARC), provided by NASA's Goddard Space Flight Center and from the UK Swift Science Data Centre at the University of Leicester.

APPENDIX

A. ADDITIONAL PLOTS

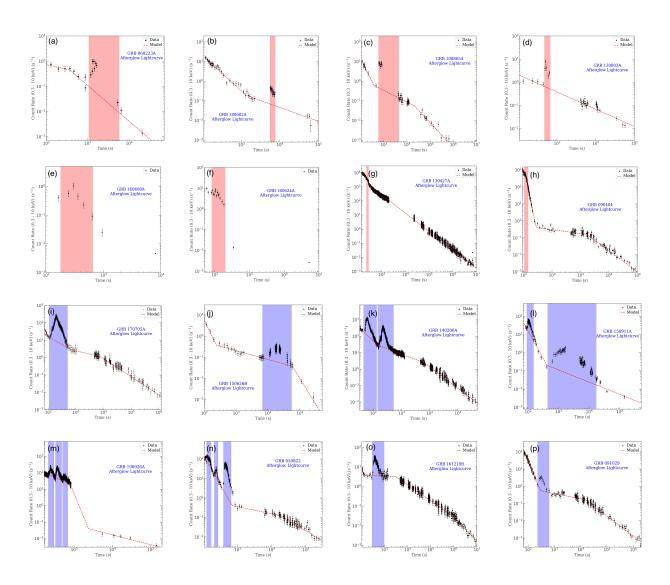


Figure 7. The afterglow lightcurves of (a) GRB 060223A and (b) GRB 180602A represent cases with no data during the decay and rise phases of the flaring episode respectively. (c) GRB 100805A and (d) GRB 130803A represent cases that have less observational points during flare emission. (e) GRB 160408A and (f) GRB 160624A represent cases where the underlying afterglow emission is absent or not enough data points are available for proper modelling. (g) GRB 130427A and (h) GRB 090404 represent cases that are avoided due to their very low signal-to-noise ratio. The red shaded portion represents the flare duration as identified by the Swift XRT team. The afterglow lightcurves of (i) GRB 170705A and (j) GRB 150626B possessing a single flare are shown. (k) GRB 140206A and (l) GRB 150911A represents afterglows with double flaring episodes, while, (m) and (n) show lightcurves of GRB 190926A and GRB 050822, which have three flaring episodes each. (o) and (p) represent lightcurves of GRB 161219B and GRB 091029 with a full and partial flare, respectively, within the plateau region of their afterglow. The blue-shaded region represents the flare duration as identified in this study. The red dotted line shown in all the plots represents the afterglow model obtained after excluding the flare region.

B. COMPARING THE PROMPT EMISSION OF GRBS WITH AND WITHOUT X-RAY FLARES

Not all GRBs detected by Swift possess X-ray flares in their afterglow emission. Thus, in order to understand if there exists any difference in the type of GRBs giving rise to flares, we made comparison plots of the distributions of different prompt emission properties such as isotropic burst energy, E_{iso} estimated for known redshift cases, T_{90} , low energy power-law spectral index, α and energy fluence of GRBs with and without X-ray flares as shown in Figure 8. Furthermore, to assess if both the sample distributions originate from the same population, we conducted a Kolmogorov–Smirnov(KS) test¹¹ on the distributions of the different parameters. The null hypothesis assumes both the flare and non-flare GRB's properties are sampled from the same underlying population and the alternate is they are not identical. The resultant p-value if lower than the probability p = 0.01 (chosen threshold), allows us to reject the null hypothesis and adopt the alternate hypothesis at a statistical significance greater than 99%. However, for the distributions of E_{iso} , T_{90} , α and energy fluence in 15 – 150 keV, we find the p-values from the KS test to be 0.17, 0.07, 0.69 and 0.03 respectively. Since the p-values lie above the threshold, we conclude that there is no particular distinction between the population of GRBs that produce and that does not produce late time X-ray flares.

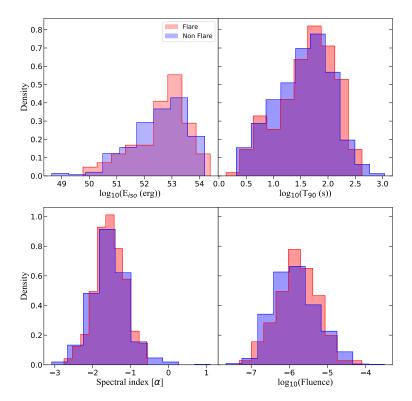


Figure 8. Comparison of the distribution of the prompt emission properties such as E_{iso} , T_{90} , α and energy fluence of GRBs with and without X-ray flares are shown.

¹¹ The scipy package ks_2samp was used.

C. TABLE OF PROMPT & X-RAY FLARE PROPERTIES

The complete catalog of the studied parameters of the sample is made available online in the machine-readable format. A sample of the catalog is shown in Table 2 for guidance regarding its form and content.

Table	2 .	catal	log
-------	------------	-------	-----

GRB	Flare	$T_{P,100}$	$T_{P,Var}$	$T_{P,Peak}$	BFM [I]	$\alpha_P [I]$	Fluence $_P$	$Fluence_P$	BFM [P]	α_P [P]	$F_{P,Peak}$	$F_{P,Peak}$	$T_{F,100}$	$T_{F,Var}$	$T_{F,Peak}$	T_q	S/N	α_F	$F_{F,Peak}$	$Fluence_F$
NAME	Episode	(s)	(s)	(s)			[15-150keV]	[0.3-10keV]			[0.3-10keV]	[15-150keV]	(s)	(s)	(s)	(s)			[0.3-10keV]	[0.3-10keV]
							$(\times 10^{-6} \text{erg/cm}^2)$	$(\times 10^{-6} \text{erg/cm}^2)$			$(\times 10^{-8} \text{erg/cm}^2/\text{s})$	$(\times 10^{-8} erg/cm^{2}/s)$							$(\times 10^{-10} \text{erg/cm}^2)$	$(\times 10^{-8} \text{erg/cm}^2)$
170208B [†]	1	32.4±2.4	0.31	1.0	PL	$-1.50^{+0.01}_{-0.01}$	4.84±0.37	1.52±0.13	PL	$-1.08^{+0.03}_{-0.02}$	$6.76^{+0.47}_{-0.44}$	$74.27^{+1.40}_{-1.39}$	172.2±31.4	6.37	98.1	70.5±3.37	28.9	$-2.88^{+0.03}_{-0.03}$	338.86 ± 44.40	46.55±8.53
140419A	1	124.6 ± 9.3	0.36	51.4	PL	$-1.02^{+0.10}_{-0.10}$	15.6±1.2	1.2 ± 0.1	PL	$-1.02^{+0.04}_{-0.04}$	$3.24^{+0.38}_{-0.32}$	$42.89^{+1.25}_{-1.30}$	106.3 ± 9.9	10.84	209.9	60.1 ± 10.6	6.0	$-1.42^{+0.16}_{-0.16}$	22.45±5.00	4.50 ± 0.96
121125A	1	78.2 ± 7.9	1.07	36.6	PL	$-1.54^{+0.03}_{-0.03}$	4.37 ± 0.44	1.52 ± 0.18				$21.43^{+1.02}_{-1.08}$	44.5±7.4	18.9	92.0	15.7 ± 8.0	5.3	$-1.76^{+0.13}_{-0.14}$	22.07 ± 4.42	2.73 ± 0.56
$190926A^{\dagger}$	1	130.1 ± 12.0	130.10	53.0	PL	$-2.06^{+0.11}_{-0.10}$	1.46 ± 0.17	2.74 ± 0.89	PL	$-2.03^{+0.40}_{-0.40}$	$5.86^{+15.57}_{-3.89}$	$3.56^{+0.78}_{-1.15}$	85.5 ± 6.6	14.36	242.1	78.5 ± 12.58	11.5	$-1.07^{+0.07}_{-0.07}$	79.21 ± 13.81	16.51 ± 1.61
190926A	2												145.2 ± 6.3	9.19	361.4	194.1 ± 12.5	12.3	$-1.35^{+0.04}_{-0.04}$	86.43 ± 13.01	34.59 ± 1.87
190926A	3												178.9 ± 18.9	81.75	584.5	370.4 ± 15.3	5.0	$-2.03^{+0.06}_{-0.06}$	22.74 ± 4.83	11.15 ± 1.33
$121217A^{\dagger}$	1	101.4 ± 16.7	3.51	0.0	PL	$-1.54^{+0.04}_{-0.05}$	2.01 ± 0.34	0.71 ± 0.15	PL	$-1.30^{+0.12}_{-0.11}$	$1.75^{+0.65}_{-0.46}$	$10.39^{+0.77}_{-0.83}$	764.3 ± 2.2	6.34	737.7	237.5 ± 16.83	18.3	$-1.41^{+0.01}_{-0.01}$	146.36 ± 18.90	189.24 ± 2.15
080906	1	180.0 ± 12.4	4.37	11.0	PL	$-1.61^{+0.04}_{-0.04}$	3.65 ± 0.27	1.61 ± 0.22	PL	$-1.60^{+0.15}_{-0.15}$	$3.61^{+1.87}_{-1.21}$	$8.29^{+0.80}_{-0.89}$	103.2 ± 14.1	45.02	186.4	60.2 ± 12.95	6.0	$-2.09^{+0.05}_{-0.06}$	21.40 ± 3.70	6.52 ± 0.94
080906	2												125.1 ± 34.9	115.54	596.2	447.6 ± 24.4		$-3.30^{+0.41}_{-0.41}$		0.33 ± 0.17
$200509\mathrm{A}^\dagger$	1	40.0 ± 3.5	0.07	1.8	PL	$-1.08^{+0.10}_{-0.10}$	1.46 ± 0.15	0.13 ± 0.04	PL	$-0.58^{+0.27}_{-0.28}$	$0.25^{+0.31}_{-0.13}$	$11.65^{+1.37}_{-1.67}$	810.2 ± 20.1	2.65	824.5	220.1 ± 18.35	26.1	-1.80+0.01	293.63 ± 35.30	231.45 ± 5.98

REFERENCES

Astropy Collaboration, Price-Whelan, A. M., Lim, P. L., et al. 2022, ApJ, 935, 167, doi: 10.3847/1538-4357/ac7c74

Ayache, E. H., van Eerten, H. J., & Daigne, F. 2020, MNRAS, 495, 2979, doi: 10.1093/mnras/staa1397

Barthelmy, S. D., Barbier, L. M., Cummings, J. R., et al. 2005, SSRv, 120, 143, doi: 10.1007/s11214-005-5096-3

Beniamini, P., & Kumar, P. 2016, MNRAS, 457, L108, doi: 10.1093/mnrasl/slw003

Burgess, J. M. 2014, MNRAS, 445, 2589, doi: 10.1093/mnras/stu1925

Burrows, D. N., Hill, J. E., Nousek, J. A., et al. 2005a, SSRv, 120, 165, doi: 10.1007/s11214-005-5097-2

—. 2005b, SSRv, 120, 165, doi: 10.1007/s11214-005-5097-2

Burrows, D. N., Romano, P., Falcone, A., et al. 2005c, Science, 309, 1833, doi: 10.1126/science.1116168

Chang, X. Z., Peng, Z. Y., Chen, J. M., et al. 2021, ApJ, 922, 34, doi: 10.3847/1538-4357/ac14b6

Chincarini, G., Moretti, A., Romano, P., et al. 2007a, ApJ, 671, 1903, doi: 10.1086/521591

—. 2007b, ApJ, 671, 1903, doi: 10.1086/521591

Dainotti, M. G., Sharma, R., Narendra, A., et al. 2023, The Astrophysical Journal Supplement Series, 267, 42, doi: 10.3847/1538-4365/acdd07

Dall'Osso, S., Perna, R., Tanaka, T. L., & Margutti, R. 2017, MNRAS, 464, 4399, doi: 10.1093/mnras/stw2695

Evans, P., Beardmore, A., Page, K. L., et al. 2007, Astronomy & Astrophysics, 469, 379

Evans, P., Beardmore, A., Page, K., et al. 2009, Monthly Notices of the Royal Astronomical Society, 397, 1177

Falcone, A. D., Morris, D., Racusin, J., et al. 2007, ApJ, 671, 1921, doi: 10.1086/523296

Gibson, S. L., Wynn, G. A., Gompertz, B. P., & O'Brien,
P. T. 2018, MNRAS, 478, 4323,
doi: 10.1093/mnras/sty1363

Hascoët, R., Beloborodov, A. M., Daigne, F., & Mochkovitch, R. 2017, MNRAS, 472, L94, doi: 10.1093/mnrasl/slx143

Iyyani, S. 2018, Journal of Astrophysics and Astronomy, 39, 75, doi: 10.1007/s12036-018-9567-9

Kakuwa, J., Murase, K., Toma, K., et al. 2012, Monthly Notices of the Royal Astronomical Society, 425, 514, doi: 10.1111/j.1365-2966.2012.21490.x

King, A., O'Brien, P. T., Goad, M. R., et al. 2005, ApJL, 630, L113, doi: 10.1086/496881

Kobayashi, S., Piran, T., & Sari, R. 1997, ApJ, 490, 92, doi: 10.1086/512791

Kumar, H., Gupta, R., Saraogi, D., et al. 2022, MNRAS, 513, 2777, doi: 10.1093/mnras/stac1061

Kumar, P., & Zhang, B. 2015, PhR, 561, 1, doi: 10.1016/j.physrep.2014.09.008

Laskar, T., Berger, E., Margutti, R., et al. 2015, ApJ, 814, 1, doi: 10.1088/0004-637X/814/1/1

Lê, S., Josse, J., & Husson, F. 2008, Journal of Statistical Software, 25, 1, doi: 10.18637/jss.v025.i01

Liu, C., & Mao, J. 2019, ApJ, 884, 59, doi: 10.3847/1538-4357/ab3e75

Lü, L.-Z., Liang, E.-W., & Cordier, B. 2022, ApJ, 941, 99, doi: 10.3847/1538-4357/ac9613

MacFadyen, A. I., Woosley, S. E., & Heger, A. 2001, ApJ, 550, 410, doi: 10.1086/319698

MacLachlan, G. A., Shenoy, A., Sonbas, E., et al. 2013, MNRAS, 432, 857, doi: 10.1093/mnras/stt241

Margutti, R., Bernardini, G., Barniol Duran, R., et al. 2011, MNRAS, 410, 1064, doi: 10.1111/j.1365-2966.2010.17504.x

Mészáros, P. 2006, Reports on Progress in Physics, 69, 2259, doi: 10.1088/0034-4885/69/8/R01

Morris, D. C. 2008, PhD thesis, Pennsylvania State University

Mu, H.-J., Lin, D.-B., Xi, S.-Q., et al. 2016, ApJ, 831, 111, doi: 10.3847/0004-637X/831/1/111

- Pedregosa, F., Varoquaux, G., Gramfort, A., et al. 2011, Journal of Machine Learning Research, 12, 2825
- Peng, Z. Y., Yin, Y., Yi, T. F., Bao, Y. Y., & Wu, H. 2015, Ap&SS, 355, 95, doi: 10.1007/s10509-014-2149-7
- Poolakkil, S., Preece, R., Fletcher, C., et al. 2021, ApJ, 913, 60, doi: 10.3847/1538-4357/abf24d
- Rees, M. J., & Mészáros, P. 1998, ApJL, 496, L1, doi: 10.1086/311244
- Rousseeuw, P. J. 1987, Journal of Computational and Applied Mathematics, 20, 53, doi: 10.1016/0377-0427(87)90125-7
- Scargle, J. D., Norris, J. P., Jackson, B., & Chiang, J. 2013, ApJ, 764, 167, doi: 10.1088/0004-637X/764/2/167
- Shi, Y.-R., Ding, X.-K., Zhu, S.-Y., Sun, W.-P., & Zhang, F.-W. 2022, Universe, 8, 358, doi: 10.3390/universe8070358
- Sonbas, E., MacLachlan, G. A., Shenoy, A., Dhuga, K. S., & Parke, W. C. 2013a, ApJL, 767, L28, doi: 10.1088/2041-8205/767/2/L28

- —. 2013b, ApJL, 767, L28,doi: 10.1088/2041-8205/767/2/L28
- Swenson, C. A., Maxham, A., Roming, P. W. A., et al. 2010, ApJL, 718, L14, doi: 10.1088/2041-8205/718/1/L14
- Vianello, G., Gill, R., Granot, J., et al. 2018, ApJ, 864, 163, doi: 10.3847/1538-4357/aad6ea
- Vianello, G., Lauer, R. J., Younk, P., et al. 2015, arXiv e-prints, arXiv:1507.08343. https://arxiv.org/abs/1507.08343
- Willingale, R., Starling, R. L. C., Beardmore, A. P., Tanvir, N. R., & O'Brien, P. T. 2013, Monthly Notices of the Royal Astronomical Society, 431, 394, doi: 10.1093/mnras/stt175
- Yi, S.-X., Xi, S.-Q., Yu, H., et al. 2016, ApJS, 224, 20, doi: 10.3847/0067-0049/224/2/20
- Yi, S.-X., Yu, H., Wang, F. Y., & Dai, Z.-G. 2017, ApJ, 844, 79, doi: 10.3847/1538-4357/aa7b7b